Pollen-based reconstructions of Holocene climate trends in the eastern Mediterranean region

Esmeralda Cruz-Silva[1,*], Sandy P. Harrison[1], I. Colin Prentice[2], Elena Marinova[3], Patrick J. Bartlein[4], Hans Renssen[5], Yurui Zhang[6]

1: School of Archaeology, Geography & Environmental Science, Reading University, Whiteknights, Reading, RG6 6AH, UK
2: Georgina Mace Centre for the Living Planet, Department of Life Sciences, Imperial College London, Silwood Park Campus, Buckhurst Road, Ascot SL5 7PY, UK
3: Laboratory for Archaeobotany, Baden-Württemberg State Office for Cultural Heritage Management, Fischersteig 9, 78343 Hemmenhofen-Gaienhofen, Germany
4: Department of Geography, University of Oregon, Eugene, Oregon 97403-1251 USA
5: Department of Natural Sciences and Environmental Health, University of South-Eastern Norway, Bø, Norway
6: State Key Laboratory of Marine Environmental Science, College of Ocean & Earth Sciences, Xiamen University, Xiamen, China

*: Corresponding author

Ms for *Climate of the Past*

1 Abstract

2 There has been considerable debate about the degree to which climate has driven societal changes in the
3 eastern Mediterranean region, partly through reliance on a limited number of qualitative records of climate
4 changes and partly reflecting the need to disentangle the joint impact of changes in different aspects of
5 climate. Here, we use tolerance-weighted Weighted Averaging Partial Least Squares to derive reconstructions
6 of mean temperature of the coldest month (MTCO), mean temperature of the warmest month (MTWA),
7 growing degree days above a threshold of 0°C (GDD0) and plant-available moisture, represented by the ratio
8 of modelled actual to equilibrium evapotranspiration (α) and corrected for past CO_2 changes for 71 individual
9 pollen records from the Eastern Mediterranean region covering part or all of the interval from 12.3 ka to the
10 present. We use these reconstructions to create regional composites that illustrate the long-term trends in
11 each variable. We compare these composites with transient climate model simulations to explore potential
12 causes of the observed trends. We show that the glacial-Holocene transition and the early part of the Holocene
13 was characterised by conditions colder than present. Rapid increases in temperature occurred between ca
14 10.3 and 9.3 ka, considerably after the end of the Younger Dryas. Although the time series are characterised
15 by centennial-to-millennial oscillations, MTCO showed a gradual increase from 9 ka to the present, consistent
16 with the expectation that winter temperatures were forced by orbitally-induced increases in insolation during
17 the Holocene. MTWA also showed an increasing trend from 9 ka and reached a maximum of ca 1.5°C greater
18 than present at *ca* 4.5 and 5 ka, followed by a gradual decline towards present-day conditions. A delayed
19 response to summer insolation changes is likely a reflection of the persistence of the Laurentide and
20 Fennoscandian ice sheets; subsequent summer cooling is consistent with the expected response to insolation
21 changes. Plant-available moisture increased rapidly after 11 ka and conditions were wetter than today
22 between 10-6 ka, but thereafter α declined gradually. These trends likely reflect changes in atmospheric
23 circulation and moisture advection into the region, and were probably too small to influence summer
24 temperature through land-surface feedbacks. Differences in the simulated trajectory of α in different models
25 highlight the difficulties in reproducing circulation-driven moisture advection into the eastern Mediterranean.

1. Introduction

The Eastern Mediterranean region is a critical region for examining the long-term interactions between climate and past societies because of the early adoption of agriculture in the region, which has been widely associated with the rapid warming at the end of the Younger Dryas (Belfer-Cohen and Goring-Morris, 2011). Societal collapse and large-scale migrations have been associated with climates less favourable to agriculture during the 8.2 ka event (Weninger et al., 2006) or to major changes in agricultural practices (Roffet-Salque et al., 2018). Subsequent periods of less favourable climate, particularly prolonged droughts, have been associated with the fall of the Akkadian empire ca. 4.2 ka (Cookson et al., 2019), and the end of the Late Bronze Age and the beginning of the Greek Dark Ages ca 3.2 ka (Kaniewski et al., 2013; Drake, 2012). However, the attribution of changes in human society to climate changes is not universally accepted. Flohr et al. (2016), for example, analysed radiocarbon-dated archaeological sites for evidence of societal changes in response to climate changes in the early Holocene, particularly the 8.2 ka event, and found no evidence of large-scale site abandonment or migration although there were indications of local adaptations. However, since Flohr et al. (2016) did not compare the archaeological records to region-specific climate reconstructions, it is difficult to assess how far local responses might reflect differences in climate between the sites. Even the societal response to the early Holocene warming appears to have differed across the region (Roberts et al., 2018).

The need to understand the interactions between climate and past societies in the Eastern Mediterranean is given further impetus because human modification of the landscape has the potential to affect climate directly through changes in land-surface properties. The degree to which human modifications of the landscape had a significant impact on global climate before the pre-industrial period is debated (Ruddiman, 2003; Joos et al., 2004; Kaplan et al., 2011; Singarayer et al., 2011; Mitchell et al., 2013; Stocker et al., 2017), but these impacts were likely to be more important in regions with a long history of settlement and agricultural activities (Harrison et al., 2020).

Much of our current understanding of climate changes in the Eastern Mediterranean region is based on the qualitative interpretation of individual records (e.g. Roberts et al., 2019). Oxygen-isotope records from speleothems or lake sediments have been used to infer changes in moisture availability through the Holocene (e.g. Bar-Matthews et al., 1997; Cheng et al., 2015; Dean et al., 2015; Burstyn et al., 2019) as have pollen-based reconstructions of changes in vegetation (e.g. Bottema, 1995; Denèfle et al., 2000; Sadori et al., 2011). Pollen records can also be used to make quantitative reconstructions of seasonal temperatures, and precipitation or plant-available water (Bartlein et al., 2011; Chevalier et al., 2020). Quantitative reconstructions of past climates have been made for individual records from the Eastern Mediterranean region (e.g. Cheddadi and Khater, 2016; Magyari et al., 2019), and syntheses of pollen-based quantitative climate reconstructions have included sites from this region (Davis et al., 2003; Mauri et al., 2015; Herzschuh et al., 2022). Davis et al. (2003) provided a composite curve of seasonal temperature changes, but not moisture changes; both summer and winter temperatures showed very little variation (<1°C) through most of the Holocene. Mauri et al. (2015) is an updated version of the Davis et al. (2003) reconstructions, with more sites included but showing similarly muted temperate changes in the Eastern Mediterranean region. Herzschuh et al. (2022) showed more homogenous changes in both temperature and precipitation across the Eastern Mediterranean region but it is difficult to compare the two reconstructions directly because they used different reconstruction techniques. None of the existing reconstructions take account of the impact of changing CO_2 levels on vegetation which could potentially affect the reconstructions of moisture variables (Prentice et al., 2022). Thus, there is a need for well-founded reconstructions of climate, particularly climate

68 variables that are relevant for human occupation and agriculture, to be able to address questions about the
69 interactions between climate and society in the Eastern Mediterranean region.

70 Here, we provide new quantitative reconstructions of seasonal temperature and plant-available moisture for
71 71 sites from the Eastern Mediterranean region (defined by the Eastern Mediterranean-Black Sea-Caspian
72 Corridor, EMBSeCBIO, project as the region between 20°E – 62°E, 29°N – 49°N), including a correction for the
73 impact of changing CO_2 levels on plant-available moisture reconstructions. We use these reconstructions to
74 document the regional trends in climate from 12.3 ka to the present. We then explore how far these trends
75 can be explained by changes in external forcing by comparing the reconstructions with transient climate model
76 simulations.

77

2. Methods

2.1. Modern pollen and climate data

80 The modern pollen dataset was obtained from version 1 of the SPECIAL Modern Pollen Data Set (SMPDSv1,
81 Harrison, 2019), which provides relative abundance data from 6459 terrestrial sites from Europe, the Middle
82 East and northern Eurasia, assembled from multiple public sources or provided by the original authors. The
83 SMPDS pollen records have been taxonomically standardized, filtered to remove obligate aquatics,
84 insectivorous species, introduced species, or taxa that only occur in cultivation. The removal of cultivars is
85 designed to minimise the influence of anthropogenic signals on the reconstructions. We then grouped taxa
86 with only sporadic occurrences into higher taxonomic levels (genus, sub-family or family). Consequently, the
87 data set provides relative abundance data for 247 pollen taxa (Supplementary Table 1). We used the 5840
88 SMPDS sites from the area between 20°W to 62°E and 29°N and 75°N to construct the training data set
89 (Supplementary Figure 1); the sampling outside this box is limited and likely not representative of the diversity
90 of the climate gradients. At sites with multiple modern samples, we averaged the taxon abundances across all
91 samples, to minimise over-representation of some localities and hence specific climates, in the training
92 dataset. We used the 195 pollen taxa that occurred at more than 10 sites (Supplementary Table 1) to derive
93 climate-abundance relationships.

94 We focus on reconstructing bioclimatic variables that fundamentally control plant distribution, specifically
95 related to winter temperature limits, accumulated summer warmth and plant-available moisture (Harrison et
96 al., 2010). The bioclimatic data for each modern site was obtained from Harrison et al. (2019), a dataset that
97 provides estimates of mean temperature of the coldest month (MTCO), growing degree days above a base
98 level of 0°C (GDD0), and a moisture index (MI) defined as the ratio of annual precipitation to annual potential
99 evapotranspiration at each modern pollen site, derived using a geographically-weighted regression of version
100 2.0 of the Climate Research Unit (CRU) long-term gridded climatology at 10 arc minute resolution (CRU CL
101 v2.0; New et al., 2002). MTCO and GDD0 were taken directly from the data set. Since Harrison et al. (2019) do
102 not provide mean temperature of the warmest month (MTWA), we calculated this based on the relationship
103 between MTCO and GDD0 given in Wei et al. (2021). We derived an alternative moisture index, α, which is the
104 ratio between modelled actual and equilibrium evapotranspiration, from MI following Liu et al. (2020). MI and
105 α both provide good indices of plant-available moisture, but since α has a natural limit in wetter conditions it
106 is more suitable for discriminating differences in drier climates.

2.2. Fossil pollen data

The fossil pollen dataset for eastern Mediterranean region was obtained from the Eastern Mediterranean-Black Sea Caspian Corridor (EMBSeCBIO) database (Harrison et al., 2021), which contains information from 187 records from the region between 20°E and 62°E and between 29°N and 49°N. (Note this is a more limited region than used for the modern training data set.) We discarded records (a) from marine environments or very large lakes (>500 km^2), (b) with no radiocarbon dating, (c) where the age of the youngest pollen sample was unknown, (d) where there is an hiatus after the youngest radiocarbon date, (e) where more than half of the radiocarbon dates were rejected by the original authors, and (f) where more than half of the ages were based on pollen correlation with other radiocarbon-dated records. However, we kept records where there is an hiatus but where there are sufficient radiocarbon dates above the hiatus to create an age model for the post-hiatus part of the record. We constructed new age models for all the remaining sites (121) using the IntCal20 calibration curve (Reimer et al., 2020) and the 'rbacon' R package (Blaauw et al., 2021) in the framework of the 'AgeR' R package (Villegas-Diaz et al., 2021). Some of these records have no modern samples, where modern was defined as 0-300 yr BP, and thus could not be used to calculate climate anomalies. As a result, 71 pollen records (Figure 1; Supplementary Table 2) were used for the climate reconstructions. These records have a mean length of 6594 years and a mean resolution of 228 years. The records were taxonomically standardized for consistency with the training dataset.

2.3 Climate reconstructions

We used tolerance-weighted Weighted Averaging Partial Least Squares (*fx*TWA-PLS, Liu et al., 2020) regression to model the relationships between taxon abundances and individual climate variables in the modern training dataset and then applied these relationships to reconstruct past climate using the fossil assemblages. *fx*TWA-PLS reduces the known tendency of regression methods to compress climate reconstructions towards the middle of the sampled range by applying a sampling frequency correction to reduce the influence of uneven sampling of climate space, and by weighting the contribution of individual taxa according to their climate tolerance (Liu et al., 2020). Version 2 of *fx*TWA-PLS (*fx*TWA-PLS2, Liu et al., 2023), applied here, uses P-spline smoothing to derive the frequency correction and also applies the correction both in estimating climate optima and in the regression itself, producing a further improvement in model performance relative to version 1 as published by Liu et al. (2020).

We evaluated the *fx*TWA-PLS models by comparing the reconstructions against observations using pseudo-removed leave-out cross-validation, where one site was randomly selected as a test site and geographically and climatically similar sites (pseudo sites) were removed from the training set to avoid redundancy in the climate information inflating the cross-validation. We selected the last significant component (*p*-value ≤ 0.01) and assessed model performance using the root mean square error of prediction (RMSEP). The degree of compression was assessed using linear regression and local compression was assessed by loess regression (*locfit*). Climate reconstructions were made for every sample in each fossil record using the best models and sample specific errors were estimated via bootstrapping. We applied a correction factor (Prentice et al., 2022) to the reconstructions of α to account for the impact of changes in atmospheric CO_2 levels on water-use efficiency, specifically the increased water use efficiency under high CO_2 levels characteristic of the recent past and the low CO_2 levels that would have reduced water use efficiency during the late glacial and thus could have influenced the reconstructions during the earliest part of the records. The correction was implemented through the package codos: 0.0.2 (Prentice et al., 2022) with past CO_2 concentration values derived from the EPICA Dome C record (Bereiter et al., 2015).

2.4. Construction of climate time series

To obtain climate time series representative of the regional trends in climate, we first screened the reconstructions to remove individual samples with (a) low effective diversity (< 2) as measured using Hill's N2 diversity measure (Hill, 1973), which could indicate low pollen counts or local contamination, and (b) sample-specific errors above the 0.95 quantile to remove obvious outliers. This screening resulted in the exclusion of only a small number of individual samples (see Supplementary Figure 2). We then averaged the reconstructed values in 300-year bins (slightly larger than the average resolution of the records, 228 years) with 50% overlap. The first bin centred on 150 yr BP, and subsequent bins were centred at 150 yr increments throughout the record. We excluded any bins with only one sample. The binned values of individual sites were averaged to produce a regional composite of the anomalies for each climate variable, where the modern baseline was taken as the first 300-yr bin centred on 150 yr BP. These time series were smoothed using locally weighted regression (Cleveland & Devlin, 1988) with a window width of 1000 years (half-window width 500 years) and fixed target points in time to highlight the long-term trends. Confidence intervals (5th and 95th percentiles) for each composite were generated by bootstrap resampling by site over 1000 iterations. We examined the impact of the CO_2 correction on reconstructed α (Supplementary Figure 3); this had no major effect on the reconstructed trends except during the earliest part of the record.

2.5. Climate model simulations

We compared the reconstructed climate changes with transient climate model simulations of the response to external forcing, to determine the extent that the reconstructed climate changes reflect changes in known forcing. We used transient simulations of the response to orbital and greenhouse gas forcing in the later Holocene from four models participating in the PAleao-Constraints on Monsoon Evolution and Dynamics (PACMEDY) project (Carré et al., 2021): the MPI (Max Planck Institute) Earth System Model version 1.2 (Dallmeyer et al., 2020), the AWI (Alfred Wegener Institute) Earth System Model version 2 (Sidorenko et al., 2019), and two versions of the IPSL (Institut Pierre Simon Laplace) Earth System Model. The IPSL and AWI simulations were run from 6 ka to 1950 CE, the MPI simulation from 7.95 ka to 1850 CE. We used a longer transient simulation covering the period from 11.5 ka made with the LOVECLIM model (Goosse et al., 2010) which, in addition to orbital and greenhouse gas forcing, accounts for the waning of the Laurentide and Fennoscandian ice sheets (Zhang et al., 2016). Finally, we used two transient simulations from 22 ka to present made using the Community Climate System Model (CCSM3; Collins et al., 2006). Both were forced by changes in orbital configuration, atmospheric greenhouse gas concentrations, continental ice sheets and meltwater fluxes, but differ in the configuration of the meltwater forcing applied after the Bølling warming (14.7 ka). In the first simulation (TRACE-21k-I: Liu et al., 2009), there was a sustained meltwater flux of ~0.1 Sv from the Northern Hemisphere ice sheets to the Arctic and North Atlantic until ca 6 ka, and a continuous inflow of water from the North Pacific into the Arctic after the opening of the Bering Strait. The second simulation (TRACE-21k-II; He and Clark, 2022) had no meltwater flux during the Bølling warming or the Holocene but applied a flux of ~ 0.17 Sv to the North Atlantic during the Younger Dryas (12.9-11.7 ka). The difference in meltwater forcing results in a much stronger Atlantic Meridional Overturning Circulation during the Holocene in the TRACE-21k-II simulation compared to the TRACE-21k-I simulation. Details of the model simulations are given in Supplementary Table 3. The use of multiple simulations allows the identification of robust signals that are not model-dependent (see e.g. Carré et al., 2021) and also the separation of the effects of different forcings. The TraCE-21k-I data were adjusted to reflect the changing length of months during the Holocene, (related to the eccentricity of Earth's orbit and the precession-determined time of year of perihelion), whereas the other

191 simulations were not. However, this makes little practical difference for the selection of variables used here
192 (Supplementary Figure 4).

193 Outputs from each simulation were extracted for land grid cells in the EMBSeCBIO domain (20° E – 55° E, 29° N
194 – 49° N; this region extends slightly less far eastwards than the EMBSeCBIO region as originally defined but
195 there are no pollen sites beyond 55° E). MTCO and MTWA were extracted directly; GDD0 was obtained by
196 deriving daily temperature values from monthly data using a mean-preserving autoregressive interpolation
197 function (Rymes & Myers, 2001). Daily values of cloud cover fraction and precipitation were obtained from
198 monthly data in the same way, and used to estimate MI, i.e. the ratio of annual precipitation to annual
199 potential evapotranspiration, through the R package smpds (Villegas-Diaz & Harrison, 2022) before converting
200 this to α following Liu et al. (2020). For consistency with the reconstructed time series, climate anomalies for
201 30-yr bins for each land grid cell within the EMBSeCBIO domain were calculated using the interval after 300 yr
202 BP as the modern baseline. Since the spatial resolution of the models varies (Supplementary Table 3), and in
203 any case is coarser than the sampling resolution of the individual pollen records precluding direct comparisons
204 except at a regional scale, we used all of the land grid cells within the EMBSeCBIO domain and did not attempt
205 to select grid cells coincident with the location of pollen data. A composite was produced by averaging the
206 grid cell time series, which was then smoothed using locally weighted regression (Cleveland & Devlin, 1988)
207 with a window width of 1000 years (i.e. a half-window width of 500 years) and fixed target points in time.
208 Confidence intervals (5th and 95th percentiles) for each composite were generated by bootstrap resampling
209 by grid cell over 1000 iterations.

3. Results

3.1.   Performance of the fxTWA-PLS statistical model

212 The assessment of the model through cross-validation showed that it reproduces the modern climate variables
213 reasonably well (Table 1, Supplementary Table 4). The best performance is achieved by α (R^2 = 0.73, RMSEP =
214 0.15) and MTCO (R^2 = 0.73, RMSEP 3.7˚). The models for GDD0 (R^2 = 0.69, RMSEP = 880) and MTWA (R^2 = 0.63,
215 RMSEP = 3.22) were also acceptable. The slopes of the regressions ranged from 0.78 (MTWA) to 0.86 (MTCO),
216 indicating that the degree of compression in the reconstructions in small (Table 1). Thus, the downcore fxTWA-
217 PLS reconstructions of all the climate variables can be considered to be robust and reliable.

3.2.   Holocene climate evolution in the region

219 Down-core reconstructions showed broadly coherent signals, although there was variation in both the timing
220 and magnitude of climate changes across the sites, reflecting differences in latitude and elevation (Figures 2,
221 3, 4). Nevertheless, the records indicated coherent regional trends over the past 12 ky.

222 Winter temperature showed a cooling trend between 12 and 11 ka, with reconstructed MTCO ca 8°C lower
223 than present at 11 ka (Figure 5). There was a moderate increase in MTCO after 11 ka, followed by a more
224 pronounced increase of ca 5°C between 10.3 and 9.3 ka. Winter temperatures were only ca 2°C lower than
225 present at the end of this rapid warming phase. There are relatively large uncertainties on the MTCO
226 reconstructions prior to 10.3 ka, so the trends in the early part of the record are not well constrained. However,
227 the phase of rapid warming between 10.3 and 9.3 ka (and the subsequent part of the record) is well
228 constrained. MTCO continued to increase gradually through the Holocene, although multi-centennial to
229 millennial oscillations were superimposed on the general trend.

230 The initial trends in summer temperature were broadly similar to those in MTCO, with a cooling between 12.3
231 and 11ka and reconstructed MTWA ca 2°C lower than present at 11 ka (Figure 5). Summer temperature

232 increased thereafter, albeit with pronounced millennial oscillations, up to ca 4.5 ka when MTWA was *ca* 1.5°C
233 higher than present. There was a gradual decrease in summer temperature after ca 4.5 ka. The GDD0
234 reconstructions showed similar trends to MTWA, reaching maximum values around 4.5 ka when the growing
235 season was ca 150 degree days greater than today. The subsequent decline in GDD0 was somewhat flatter,
236 which presumably reflects the influence of still-increasing winter temperatures on the length of the growing
237 season.

238 The trends in α differ from the trends in temperature. Conditions were similar to present around 11.5 ka
239 (Figure 5). Between 11 and 10 ka, there was a rapid increase in α. Values of α were higher than present (>0.1)
240 between 10 to 6 ka. Subsequently, there was a gradual and continuous decrease in α until the present time.
241 The correction for the physiological impact of CO_2 levels was, as expected, largest during intervals when CO_2
242 was lowest (i.e. prior to 11 ka) (Supplementary Figure 4). The reconstructions with and without the correction
243 are not statistically different between 10 and 5 ka, taking account the uncertainties in the reconstructions, but
244 the correction produced marginally wetter reconstructions after 5 ka, with a maximum difference of 0.08.
245 However, the gradually declining trend in moisture availability towards the present is not affected by the CO_2
246 correction.

3.3. Comparison with climate simulations

248 The TRACE-21k-I simulation (Figure 6) shows an initial winter warming between 12-11 ka but MTCO is still ca
249 3°C lower than present at 11 ka. There is a gradual increase in MTCO from 11 ka onwards, although with
250 centennial-scale variability and a more pronounced oscillation corresponding to the 8.2 ka event. The TRACE-
251 21k-II simulation is initially slightly colder and displays a two-step warming with a peak at 8.5 ka, when MTCO
252 is ca 1.5°C lower than present. The later Holocene trend is similar to that shown in TRACE-21k-I. The LOVECLIM
253 simulation produced generally warmer conditions than either of the TRACE simulations: MTCO is ca 2.5°C
254 lower than present at 11 ka but the two-step warming is more pronounced and peak warming occurs
255 somewhat later at ca 7.5 ka when MTCO was only ca 0.25°C lower than present (Figure 7). While all three
256 models show a rapid warming comparable to the reconstructed warming between 10.3 and 9.3 ka, it is clear
257 that differences in the ice sheet and meltwater forcings affect both the magnitude and the timing of this trend.
258 The overall magnitude of the warming after 9 ka in the TRACE-21k-I simulation is consistent with the
259 reconstructions of MTCO (anomalies of 2.4°C and 2.6°C for model and data respectively). The mid-to late
260 Holocene trend is similar in the PACMEDY simulations (Figure 8) to both TRACE-21k simulations, both in sign
261 and in magnitude (ca 1°C between 6 ka and present) and both are consistent with the reconstructions (−0.9 ±
262 0.7°C). The continuous increase of MTCO is consistent with the change in winter insolation. Given the
263 similarities between the PACMEDY simulations (which only include orbital and greenhouse gas forcing) and
264 the LOVECLIM and TRACE simulations, which also include forcing associated with the relict Laurentide and
265 Fennoscandian ice sheets, it seems likely that orbital forcing was the main driver of winter temperatures in
266 the EMBSeCBIO region during the later Holocene.

267 The TRACE-21k-I simulation shows peak summer temperatures between 11-9 ka, when MTWA was ca. 3°C
268 greater than present (Figure 6). The TRACE-21K-II simulations is initially colder than the TRACE-21k-I
269 simulation and the peak in summer temperatures occurs at 9 ka, when MTWA was ca 2.5°C greater than
270 present (Figure 6). The LOVECLIM simulation is warmer than present from 11.5 ka, but peak warming is only
271 reached at 7.5 ka when MTWA is ca 2°C (Figure 7). All three simulations show a gradual decrease in summer
272 temperature through the Holocene after this initial peak. This decreasing trend is also seen in the PACMEDY
273 simulations from 6 ka (or 8 ka in the case of the MPI simulation) onwards (Figure 8) and the magnitude of the
274 change over this interval (ca 2°C from 6ka onwards) is similar to that shown by the TRACE and the LOVECLIM

simulations. This similarity suggests that the simulated response is a direct reflection of the change in orbital forcing. However, the reconstructed changes in summer temperature do not show this gradual decline. Reconstructed MTWA is ca 4°C colder than the model predictions at 9 ka. The reconstructions show a gradual increase in MTWA from 9 to 4.5 ka. Changes in reconstructed temperatures at 4.5 ka are of a similar magnitude to simulated temperatures at this time (ca 1°C greater than present) although the late Holocene is marked by a cooling trend as seen in the simulations. Thus, while the simulated late Holocene trend is consistent with orbital forcing being the main driver of summer temperatures in the EMBSeCBIO region, the early to mid-Holocene trend is not. Previous modelling studies have suggested that the timing of peak warmth differs in different regions of Europe and is associated with the impact of the Fennoscandian ice sheet on regional climates (Renssen et al., 2009; Blascheck and Renssen, 2013; Zhang et al., 2016). The differences in the timing of peak warmth in the EMBSeCBIO region in the TRACE-21k-II and LOVECLIM simulations would be consistent with this argument but suggest that the timing and magnitude are model-dependent. It is therefore plausible that the reconstructed trend in MTWA at least during the early Holocene reflects the influence of the relict Laurentide and Fennoscandian ice sheets in modulating the impact of increased summer insolation until the mid-Holocene. Given that GDD0 is a reflection of both changes in season length, as influenced by winter temperatures, and summer warming, the difference between simulated and reconstructed MTWA are also seen in GDD0 trends during the early part of the Holocene (Figure 6).

The simulations do not show consistent patterns for the trend in α. The TRACE-21k-I simulation (Figure 6) shows a gradual increase, with minor multi-centennial oscillations from 12 ka to present. (Available model output variables are not sufficient to calculate α for the TRACE-21k-II or LOVECLIM simulations). One of the PACMEDY simulations (IPSL-CM5) shows an increase from the mid-Holocene (Figure 8) although the simulated change is an order of magnitude smaller than over the comparable period in the TRACE-21k-I simulation. The AWI model shows no trend in α over this period; the remaining two models show increasing aridity from the mid-Holocene to present (Figure 8). These three models are all broadly consistent with the reconstructions since the reconstructed decrease in α is small. However, the differences in the sign of the trend between the different models indicates that changes in moisture are not a straightforward consequence of the forcing, but must reflect model-dependent changes in moisture supply via changes in atmospheric circulation. Reconstructions of Holocene climates in Iberia have suggested that land-surface feedbacks associated with changes in moisture availability have a strong influence on summer temperature (Liu et al., 2023). There does not seem to be strong evidence for this in the EMBSeCBIO region, given the difference in the trends of α and MTWA and the muted nature of the trend in α.

4. Discussion

The three temperature-related variables, MTCO, MTWA and GDD0 all show relatively warm conditions around the late glacial/Holocene transition (ca 12 ka) followed by a cooling that was greatest between *ca* 11 and 10 ka. This pattern is also shown in regional composites (Figure 9) derived from the reconstructions by Mauri et al. (2015) and Herzschuh et al. (2022). However, the magnitude of the cooling shown in the Mauri et al. (2015) and Herzschuh et al. (2022) reconstructions is small compared to our reconstructions. The cool interval starts somewhat later and persists until 9 ka in the Mauri et al. (2015) reconstructions, but this is partly a reflection of the fact that these reconstructions were only made at 1 ka intervals and thus the transitions are less well constrained than in either our reconstructions or those of Herzschuh et al. (2022). This cool interval and the marked warming seen after 10.3 ka in our reconstructions, does not correspond to the Younger Dryas and the

subsequent warming. Although the Younger Dryas is considered to be a globally synchronous event (Cheng et al., 2020) and is generally considered coeval with Greenland Stadial I (Larsson et al., 2022), it does not appear to be strongly registered in the EMBSeCBIO region in any of the quantitative climate reconstructions. This is consistent with earlier suggestions based on vegetation changes that the Younger Dryas was not a clearly marked feature over much of this region (Bottema, 1995).

We have shown that winter temperatures increased sharply between 10.3 and 9.3 ka, but then continued to increase at a more gradual rate through the Holocene. The increase of ca 7.5°C is of the same order of magnitude to the increase shown in the TRACE-21K-II simulation (ca. 5°C) and in the LOVECLIM simulation (ca. 3°C). This increasing trend is also seen in the Mauri et al. (2015) reconstructions of MTCO (Figure 9), although the change from the early Holocene to the present is much smaller (ca 0.5–1°C) in these reconstructions than in our reconstructions and Mauri et al. (2015) do not show marked cooling around 11 ka. Nevertheless, the consistency between the two reconstructions and between our reconstruction and the simulated changes in MTCO supports the idea that these trends are a response to orbital forcing during the Holocene. Our reconstructions show a gradual increase in summer temperature, as measured by both MTWA and GDD0, from *ca* 10 to 5 ka when MTWA was ca 1°C warmer than present, followed by a gradual decrease towards the present. This is not consistent with previous reconstructions. Mauri et al. (2015) show an overall increasing trend from 9 ka to present. The Herzschuh et al. (2022) shows a completely different pattern, with the maximum in July temperature at ca. 9 ka and an oscillating but declining trend thereafter (Figure 9).

These differences between the three sets of reconstructions are too large to be caused by differences in the age models applied. They are also unlikely to reflect differences in sampling, since the number of sites used is roughly similar across all three reconstructions (71 sites versus 67 sites from Herzschuh et al., 2022 and 409 grid points, based on 57 sites, from Mauri et al., 2015); most sites are common to all three analyses. The differences must therefore be related to the reconstruction method. Herzshuch et al. (2022) used the regression-based approach, Weighted Average Partial Least Squares (WA-PLS), that is the basis for our reconstruction technique, fxTWA-PLSv2. Mauri et al. (2015) used the modern analogue technique. However, after taking account of differences caused by the temporal resolution, there is greater similarity between our reconstructions and those of Mauri et al. (2015) than between either of these reconstructions and the Herzschuh et al. (2022) reconstructions.

Several methodological issues could be responsible for the differences between the three sets of reconstructions, and in particular the anomalous moisture trends shown by Herzschuh et al. (2022). Specifically, Herzschuh et al. (2022) used (1) a unique calibration data set for each fossil site based on modern samples within a 2000 km radius of that site, rather than relying on a single training data set; (2) a limited set of 70 dominant taxa rather than the whole pollen assemblage; and (3) included marine records from e.g. the Black Sea, which were excluded in the other reconstructions because they sample an extremely large area and thus are unrepresentative of the local climate. However, inclusion of records from the Black Sea in our reconstructions does not have a substantial impact on either the magnitude or the trends in climate. Thus, it seems likely that the differences between these two reconstructions reflects the use of a unique calibration data set for each fossil site and the limited set of taxa included.

Reconstructed MTWA shows a gradual increase through the early Holocene with maximum values of around 1.5°C greater than present reached at ca 4.5 ka. Previous modelling studies have shown the timing of maximum warmth during the Holocene in Europe was delayed compared to the maximum of insolation forcing and varied regionally as a consequence of the impact of the Fennoscandian ice sheet on surface albedo, atmospheric circulation and heat transport (Renssen et al., 2009; Blascheck and Renssen, 2013; Zhang et al.,

360   2016; Zhang et al., 2023). Two of the simulations examined here show a delay in the timing of peak warmth,
361   which occurred ca 9 ka in the TRACE-21k-II simulation and ca 7.5 ka in the LOVECLIM simulation. Although
362   both sets of simulations include the relict Laurentide and Fennoscandian ice sheets, neither has realistic ice
363   sheet and meltwater forcing. In the LOVECLIM simulation, for example, the Fennoscandian ice sheet was gone
364   by 10 ka whereas in reality it persisted until at least 8.7 ka (Patton et al., 2017). Thus, the impact of the
365   Fennoscandian ice sheet in delaying orbitally induced warming would likely have been greater than shown in
366   this simulation. In addition to differences in the way in which ice sheets and meltwater forcing are
367   implemented in different models, models are also differentially sensitive to the presence of the same
368   prescribed ice sheet (Kapsch et al., 2022). Thus, it would be useful to examine the influence of more realistic
369   prescriptions of the relict ice sheets on the climate of the EMBSeCBIO region using multiple models, and
370   preferably transient simulations at higher resolution or regional climate models. It has been suggested that
371   meltwater was routed to the Black and Caspian Seas via the Dnieper and Volga Rivers during the early phase
372   of deglaciation (e.g. Yanchilina et al., 2019; Aksu et al. 2022; Vadsaria et al., 2022) and it would also be useful
373   to investigate the impact of this on the regional climate.

374   We have shown that α was similar to today around 11 ka, but there was a rapid increase in moisture availability
375   after ca 10.5 ka such that α values were noticeably higher than present between 10 to 6 ka, followed by a
376   gradual and continuous decrease until the present time. Changes in the late Holocene are small even at
377   centennial scale (Figure 5). The reconstructed trends in α are not captured in the simulations, which show
378   different trends during the late Holocene. Thus, it is unlikely that the gradual increase in aridity during the late
379   Holocene is a straight-forward response to orbital forcing. Changes in α in the EMBSeCBIO region are likely to
380   be primarily driven by precipitation changes, which in turn are driven by changes in atmospheric circulation.
381   Differences in the trend of moisture availability between the models imply that the nature of the changes in
382   circulation varies between models and thus the simulations do not provide a strong basis for explaining the
383   observed patterns of change in moisture availability. Earlier studies, focusing on the western Mediterranean
384   (Liu et al., 2023), Europe (Mauri et al., 2014) and central Eurasia (Bartlein et al., 2017), have shown that models
385   have difficulty in simulating the enhanced moisture transport into the Eurasian continent shown by
386   palaeoenvironmental data during the mid-Holocene and during the late Holocene. Changes in precipitation
387   can also affect land-surface feedbacks. Liu et al. (2023), for example, have argued that enhanced moisture
388   transport into the Iberian peninsula during the mid-Holocene led to more vegetation cover and increased
389   evapotranspiration and had a significant impact in reducing growing season temperatures. Differences in the
390   reconstructed trends of summer temperature and plant-available moisture through the Holocene suggests
391   that this land-surface feedback was not an important factor influencing summer temperatures in the
392   EMBSeCBIO region. Nevertheless, differences in the strength of land-surface feedbacks between models could
393   also contribute to the divergences seen in the simulations. It would be useful to investigate the role of changes
394   in atmospheric circulation for precipitation patterns during the Holocene in the EMBSeCBIO region using
395   transient simulations at higher resolution or regional climate models.

396   The timing of the transition to agriculture in the eastern Mediterranean is still debated (Asouti & Fuller, 2012).
397   It has been argued that climatic deterioration and population growth during the Younger Dryas triggered a
398   shift to farming (Weiss & Bradley, 2001; Bar-Yosef et al., 2017). The presence of morphologically altered
399   cereals by the end of the Pleistocene has been put forward as evidence for an early transition to agriculture
400   (Bar-Yosef et al., 2017), but it has also been pointed out that the evidence for cereal domestication before ca
401   10.5ka is poorly dated and insufficiently documented (Nesbitt, 2002) and that crops did not replace foraging
402   economies until well into the Holocene (Smith, 2001; Willcox, 2012; Zeder, 2011). The availability of water is
403   a crucial factor in the viability of early agriculture (Richerson et al., 2001; Zeder, 2011). We have shown that

moisture availability was higher than today during the first part of the Holocene (10-6 ka) but similar to today until ca 10. 5 ka. Wetter conditions during the early Holocene could have been a crucial factor in the transition to agriculture, and our findings support the idea that this transition did not happen until much later than the Younger Dryas or late glacial/Holocene transition. Further exploration of the role of climate in the transition to agriculture would require a more comprehensive assessment of the archaeobotanical evidence. The issue could also be addressed using modelling to explore how the reconstructed changes in regional moisture availability and seasonal temperatures would impact crop viability (see e.g. Contreras et al., 2019).

We have focused on the composite picture of regional changes across the EMBSeCBIO region, in order to investigate whether these changes could be explained as a consequence of known changes in forcing. The data set also provides information on the trends in climate at individual sites. These data could be used to address the question of whether population density or cultural changes reflect shifts in climate (e.g. Weninger et al., 2006; Drake, 2012; Kaniewski et al., 2013; Cookson et al., 2019; Weiberg et al., 2019; Palmisano et al., 2021). In addition, it would also be possible to use these data to explore the impact of climate changes on the environment, including the natural resources available for people (Harrison et al., 2023).

5. Conclusions

We have reconstructed changes in seasonal temperature and in plant-available moisture from 12.3 ka to the present from 71 sites from the EMBSeCBIO domain to examine changes in the regional climate of the eastern Mediterranean region. We show that there are regionally coherent trends in these variables. The large increase in both summer and winter temperatures during the early Holocene considerably post-dates the warming observed elsewhere at the end of the Younger Dryas, supporting the idea that the impact of the Younger Dryas in the EMBSeCBIO region was muted. Subsequent changes in winter temperature are consistent with the expected response to insolation changes. The timing of peak summer warming occurred later than expected as a consequence of insolation changes and likely, at least in part, reflects the influence of the relict Laurentide and Fennoscandian ice sheets on the regional climate. There is a rapid increase in plant-available moisture between 11 and 10 ka, which could have promoted the adoption of agriculture in the region.

442 We thank members of the SPECIAL team in Reading and from the Leverhulme Centre for Wildfires,
443 Environment and Society for useful discussions about these analyses.

444 **Financial support.**

448

References

449   **References**

450   Aksu, A. E., and Hiscott, R. N.: Persistent Holocene outflow from the Black Sea to the eastern Mediterranean
451   Sea still contradicts the Noah's Flood Hypothesis: A review of 1997–2021 evidence and a regional
452   paleoceanographic synthesis for the latest Pleistocene–Holocene, Earth Sci. Rev., 227, 103960.
453   https://doi.org/10.1016/j.earscirev.2022.103960, 2022.

454   Bar-Matthews, M., Ayalon, A., and Kaufman, A.: Late Quaternary paleoclimate in the eastern Mediterranean
455   region from stable isotope analysis of speleothems at Soreq Cave, Israel, Quat. Res., 47, 155-168,
456   https://doi.org/10.1006/qres.1997.1883, 1997.

457   Bartlein, P. J., Harrison, S.P., Brewer, S., Connor, S., Davis B.A.S., Gajewski, K., Guiot, J., Harrison-Prentice, T.
458   I., Henderson, A., Peyron, O., Prentice, I. C., Scholze, M., Seppä, H., Shuman, B., Sugita, S., Thompson, R. S.,
459   Viau, A., Williams, J., and Wu, H.: Pollen-based continental climate reconstructions at 6 and 21 ka: a global
460   synthesis, Clim. Dynam., 37, 775–802, 2011.

461   Bartlein, P.J., Harrison, S.P., and Izumi, K.: Underlying causes of Eurasian mid-continental aridity in
462   simulations of mid-Holocene climate, Geophys, Res. Lett., 44, 9020-9028, doi: 10.1002/2017GL074476, 2017.

463   Belfer-Cohen, A., & Goring-Morris, A. N. Becoming Farmers: The Inside Story. Current Anthropology, 52(S4),
464   S209–S220. https://doi.org/10.1086/658861, 2011.

465   Bereiter, B., Eggleston, S., Schmitt, J., Nehrbass-Ahles, C., Stocker, T.F., Fischer, H., Kipfstuhl, S., and
466   Chappellaz, J.: Revision of the EPICA Dome C CO_2 record from 800 to 600 kyr before present, Geophys. Res.
467   Lett., 42, 542–549, https://doi.org/10.1002/2014GL061957, 2015.

468   Bini, M., Zanchetta, G., Perşoiu, A., Cartier, R., Català, A., Cacho, I., Dean, J.R., Di Rita, F., Drysdale, R.N.,
469   Finnè, M., Isola, I., Jalali, B., Lirer, F., Magri, D., Masi, A., Marks, L., Mercuri, A.M., Peyron, O., Sadori, L., …
470   and Brisset, E.: The 4.2 ka BP Event in the Mediterranean region: An overview, Clim. Past, 15, 555–577,
471   https://doi.org/10.5194/cp-15-555-2019, 2019.

472   Bird, D., Miranda, L., Vander Linden, M., Robinson, E., Bocinsky, R.K., Nicholson, C., Capriles, J.M., Finley, J.B.,
473   Gayo, E.M., Gil, A., d'Alpoim Guedes, J., Hoggarth, J.A., Kay, A., Loftus, E., Lombardo, U., Mackie, M.,
474   Palmisano, A., Solheim, S., Kelly, RL., and Freeman, J.: P3k14c, a synthetic global database of archaeological
475   radiocarbon dates, Sci. Data, 9, 27, https://doi.org/10.1038/s41597-022-01118-7, 2022.

476   Blaauw, M., Christen, J.A., Aquino Lopez, M.A., Vazquez, J.E., Gonzalez V.O.M., Belding, T., Theiler, J., Gough,
477   B., and Karney, C.: *rbacon: Age-Depth Modelling using Bayesian Statistics* (2.5.6) [R]. https://CRAN.R-
478   project.org/package=rbacon, 2021. (last accessed 17 April 2023)

479   Blaschek, M., and Renssen, H.: The Holocene thermal maximum in the Nordic Seas: the impact of Greenland
480   Ice Sheet melt and other forcings in a coupled atmosphere-sea-ice-ocean model, Clim. Past, 9, 1629-1643,
481   10.5194/cp-9-1629-2013, 2013.

482   Bottema, S.: The Younger Dryas in the eastern Mediterranean, Quat. Sci. Rev., 14, 883-891,
483   https://doi.org/10.1016/0277-3791(95)00069-0, 1995.

484   Burstyn, Y., Martrat, B., Lopez, J. F., Iriarte, E., Jacobson, M.J., Lone, M.A., and Deininger, M.: Speleothems
485   from the Middle East: An example of water limited environments in the SISAL database. Quaternary, 2, 16.
486   https://doi.org/10.3390/quat2020016, 2019.

487   Carré, M., Braconnot, P., Elliot, M., d'Agostino, R., Schurer, A., Shi, X., Marti, O., Lohmann, G., Jungclaus, J.,
488   Cheddadi, R., Abdelkader di Carlo, I., Cardich, J., Ochoa, D., Salas Gismondi, R., Pérez, A., Romero, P.E., Turcq,

489   B., Corrège, T., and Harrison, S.P.: High-resolution marine data and transient simulations support orbital
490   forcing of ENSO amplitude since the mid-Holocene. Quat. Sci. Rev., 268, 107125.
491   https://doi.org/10.1016/j.quascirev.2021.107125, 2021.

492   Cheddadi, R., and Khater, C.: Climate change since the last glacial period in Lebanon and the persistence of
493   Mediterranean species, Quat. Sci. Rev., 150, 146-157, https://doi.org/10.1016/j.quascirev.2016.08.010,
494   2016.

495   Cheng, H., Sinha, A., Verheyden, S., Nader, F.H., Li, X.L., Zhang, P.Z., Yin, J.J., Yi, L., Peng, Y.B., Rao, Z.G., Ning,
496   Y.F., and Edwards, R.L.: The climate variability in northern Levant over the past 20,000 years, Geophys. Res.
497   Lett., 42, 8641–8650, https://doi.org/10.1002/2015GL065397, 2015.

498   Cheng, H., Zhang, H., Spötl, C., Baker, J., Sinha, A., Li, H., Bartolomé, M., Moreno, A., Kathayat, G., Zhao, J.,
499   Dong, X., Li, Y., Ning, Y., Jia, X., Zong, B., Ait Brahim, Y., Pérez-Mejías, C., Cai, Y., Novello, V.F., Cruz, F.W.,
500   Severinghaus, J.P., An, Z., and Edwards. R.L.: Timing and structure of the Younger Dryas event and its
501   underlying climate dynamics, Proc. Natl. Acad. Sci. USA, 117, 23408-23417, doi: 10.1073/pnas.2007869117,
502   2020.

503   Chevalier, M., Davis, B.A.S., Heiri, O., Seppä, H., Chase, B.M., Gajewski, K., Lacourse, T., Telford, R.J.,
504   Finsinger, W., Guiot, J., Kühl, N., Maezumi, S.Y., Tipton, J.R., Carter, V.A., Brussel, T., Phelps, L.N., Dawson, A.,
505   Zanon, M., Vallé, F., Nolan, C., Mauri, A., de Vernal, A., Izumi, K., Holmström, L., Marsicek, J., Goring, S.,
506   Sommer, P.S., Chaput, M., and Kupriyanov, D.: Pollen-based climate reconstruction techniques for late
507   Quaternary studies, Earth Sci. Rev., 210, 103384, https://doi.org/10.1016/j.earscirev.2020.103384, 2020.

508   Cleveland, W.S., and Devlin, S.J.: Locally weighted regression: An approach to regression analysis by local
509   fitting, J. Am. Stat. Assoc., 83, 596–610. https://doi.org/10.1080/01621459.1988.10478639, 1988.

510   Cookson, E., Hill, D.J., and Lawrence, D.: Impacts of long term climate change during the collapse of the
511   Akkadian Empire, J. Arch. Sci., 106, 1-9, https://doi.org/10.1016/j.jas.2019.03.009, 2019.

512   Collins, W.D., Bitz, C.M., Blackmon, M.L., Bonan, G.B., Bretherton, C.S., Carton, J.A., Chang, P., Doney, S.C.,
513   Hack, J.J., Henderson, T.B., Kiehl, J.T., Large, W.G., McKenna, D.S., Santer, B.D., and Smith, R.D.: The
514   Community Climate System Model version 3 (CCSM3), J. Clim., 19, 2122-2143,
515   http://dx.doi.org/10.1175/JCLI3761.1, 2006.
516
517   Connor, S., Colombaroli, D., Confortini, F., Gobet, E., Ilyashuk, B.P., Ilyashuk, E.A., van Leeuwen, J.F.N.,
518   Lamentowicz, M., van der Knaap, W.O., Malysheva, E., Marchetto, A., Margalitadze, N., Mazei, Y., Mitchell,
519   E.A.D., Payne, R.J., and Ammann, B.: Long-term population dynamics: Theory and reality in a peatland
520   ecosystem, J. Ecol., 106, 1, https://doi.org/10.1111/1365-2745.12865, 2017.

521   Contreras, D.A., Bondeau, A., Guiot, J., Kirman, A., Hiriart, E., Bernard, L., Suarez, R., Fader, M.: 2019. From
522   paleoclimate variables to prehistoric agriculture: Using a process-based agro-ecosystem model to simulate
523   the impacts of Holocene climate change on potential agricultural productivity in Provence, France, Quat.
524   Internat., 501, 303-316

525   Cruz-Silva, E., Harrison, S.P., Marinova, E., and Prentice, I.C.: A new method based on surface-sample pollen
526   data for reconstructing palaeovegetation patterns, J. Biogeog., 49, 1381–1396,
527   https://doi.org/10.1111/jbi.14448, 2022.

528   Dallmeyer, A., Claussen, M., Lorenz, S.J., and Shanahan, T.: The end of the African humid period as seen by a
529   transient comprehensive Earth system model simulation of the last 8000-years, Clim. Past, 16, 117–140,
530   https://doi.org/10.5194/cp-16-117-2020, 2020.

531 Davis, B.A.S., Brewer, S., Stevenson, A.C., and Guiot, J.: The temperature of Europe during the Holocene
532 reconstructed from pollen data, Quat. Sci. Rev., 22: 1701-1716, https://doi.org/10.1016/S0277-
533 3791(03)00173-2, 2003.

534 Davis, T.W., Prentice, I.C., Stocker, B.D., Thomas, R.T., Whitley, R.J., Wang, H., Evans, B.J., Gallego-Sala, A.V.,
535 Sykes, M.T., and Cramer, W.: Simple process-led algorithms for simulating habitats (SPLASH v.1.0): Robust
536 indices of radiation, evapotranspiration and plant-available moisture, Geosci. Model Dev., 10, 689–708,
537 https://doi.org/10.5194/gmd-10-689-2017, 2017.

538 Dean, J.R., Jones, M.D., Leng, M.J., Noble, S.R., Metcalfe, S.E., Sloane, H.J., Sahy, D., Eastwood, W.J., and
539 Roberts, C.N.: Eastern Mediterranean hydroclimate over the late glacial and Holocene, reconstructed from
540 the sediments of Nar lake, central Turkey, using stable isotopes and carbonate mineralogy, Quat. Sci. Rev.,
541 124, 162–174, https://doi.org/10.1016/j.quascirev.2015.07.023, 2015.

542 Denèfle, M., Lézine, A., Fouache, E., and Dufaure, J.: A 12,000-Year pollen record from Lake Maliq,
543 Albania, Quat. Res., 54, 423-432, doi:10.1006/qres.2000.2179, 2000.

544 Drake, B.L.: The influence of climatic change on the Late Bronze Age Collapse and the Greek Dark Ages. J.
545 Arch. Sci., 39, 1862–1870, https://doi.org/10.1016/j.jas.2012.01.029, 2012.

546 Flohr, P., Fleitmann, D., Matthews, R., Matthews, W., and Black, S.: Evidence of resilience to past climate
547 change in Southwest Asia: Early farming communities and the 9.2 and 8.2 ka events, Quat. Sci. Rev., 136, 23–
548 39, https://doi.org/10.1016/j.quascirev.2015.06.022, 2016.

549 Goosse, H., Brovkin, V., Fichefet, T., Haarsma, R., Huybrechts, P., Jongma, J., Mouchet, A., Selten, F., Barriat,
550 P.-Y., Campin, J.-M., Deleersnijder, E., Driesschaert, E., Goelzer, H., Janssens, I., Loutre, M.-F., Morales
551 Maqueda, M. A., Opsteegh, T., Mathieu, P.-P., Munhoven, G., Pettersson, E. J., Renssen, H., Roche, D. M.,
552 Schaeffer, M., Tartinville, B., Timmermann, A., and Weber, S. L.: Description of the Earth system model of
553 intermediate complexity LOVECLIM version 1.2, Geosci. Model Dev., 3, 603–633,
554 https://doi.org/10.5194/gmd-3-603-2010, 2010.

555 Goring-Morris, A.N., and Belfer-Cohen, A.: Evolving human/animal interactions in the Near Eastern Neolithic:
556 feasting as a case study, In G. Aranda, S. Monton, & M. Sanchez (Eds) Guess Who's Coming to Dinner.
557 Feasting Rituals in the Prehistoric Societies of Europe and Near East, pp. 64-72, Oxbow Books, Oxford, 2011.

558 Harrison, S.P.: Modern pollen data for climate reconstructions, version 1 (SMPDS) [Data set]. University of
559 Reading. https://doi.org/10.17864/1947.194, 2019. (last accessed 17 April 2023)

560 Harrison, S. P., and Prentice, I.C.: Climate and CO_2 controls on global vegetation distribution at the Last
561 Glacial Maximum: Analysis based on palaeovegetation data, biome modelling and palaeoclimate simulations,
562 Glob. Change Biol., 9, 983–1004, https://doi.org/10.1046/j.1365-2486.2003.00640.x, 2003.

563 Harrison, S. P., Marinova, E., and Cruz-Silva, E.: EMBSeCBIO pollen database [Data set]. University of Reading.
564 https://doi.org/10.17864/1947.309, 2021. (last accessed 17 April 2023)

565 Harrison, S.P., Prentice, I.C., Sutra J-P., Barboni, D., Kohfeld, K.E. and Ni. J.: Ecophysiological and bioclimatic
566 foundations for a global plant functional classification, J. Veg. Sci. 21, 300-317, doiI 10.1111/j.1654-
567 1103.2009.01144x, 2010.

568 Harrison, S.P., Gaillard, M-J., Stocker, B., Vander Linden, M., Klein Goldewijk, K., Boles, O., Braconnot, P.,
569 Dawson, A., Fluet-Chouinard, E., Kaplan, J.O., Kastner, T., Pausata, F.S.R., Robinson, E., Whitehouse, N.,
570 Madella, M., Morrison, K.D.: Development and testing of scenarios for implementing Holocene LULC in Earth

571 System Model experiments, Geosci. Model Dev., 13, 805-824, https://doi.org/10.5194/gmd-13-805-2020,
572 2020.

573 Harrison, S.P., Cruz-Silva, E., Haas, O., Liu, M., Parker, S., Qiao, S., Luke Sweeney, L., in press. Tools and
574 approaches to addressing the climate-humans nexus during the Holocene. Proceedings of the 12th ICAANE
575 Congress, Harrassowitz Verlag.

576 He, F., and Clark, P.U.: Freshwater forcing of the Atlantic Meridional Overturning Circulation revisited. Nat.
577 Clim. Change, 12, 449-454, https://doi.org/10.1038/s41558-022-01328-2, 2022.

578 Hengl, T.: Potential distribution of biomes (Potential Natural Vegetation) at 250 m spatial resolution [data
579 set], https://doi.org/10.5281/zenodo.3526620, 2019 (last accessed 17 April 2023)

580 Herzschuh, U., Böhmer, T., Li, C., Cao, X., Hébert, R., Dallmeyer, A., Telford, R.J. and Kruse, S.: Reversals in
581 temperature-precipitation correlations in the Northern Hemisphere extratropics during the
582 Holocene, Geophys. Res. Lett., 49, e2022GL099730, https://doi.org/10.1029/2022GL099730, 2022.

583 Hill, M.O.: Diversity and evenness: A unifying notation and its consequences, Ecol. 54, 427–432,
584 https://doi.org/10.2307/1934352, 1973.

585 Jalut, G., Dedoubat, J.J., Fontugne, M., and Otto, T.: Holocene circum-Mediterranean vegetation changes:
586 Climate forcing and human impact, Quat. Int., 200, 4–18, https://doi.org/10.1016/j.quaint.2008.03.012,
587 2009.

588 Joos, F., Gerber, S., Prentice, I.C., Otto-Bliesner, B.L., and Valdes, P.J.: Transient simulations of Holocene
589 atmospheric carbon dioxide and terrestrial carbon since the last glacial maximum, Glob. Biogeochem. Cy.,
590 18, GB2002, doi:10.1029/2003GB002156, 2004.

591 Kaniewski, D., Van Campo, E., Guiot, J., Le Burel, S., Otto, T., and Baeteman, C.: Environmental roots of the
592 Late Bronze Age Crisis. PLoS ONE, 8, e71004. https://doi.org/10.1371/journal.pone.0071004, 2013.

593 Kaplan, J.O., Krumhardt, K.M., Ellis, E.C., Ruddiman, W.F., Lemmen, C., and Klein Goldewijk, K.: Holocene
594 carbon emissions as a result of anthropogenic land cover change, Holocene, 21, 775-791, 2011.

595 Kapsch, M.-L., Mikolajewicz, U., Ziemen, F., and Schannwell, C.: Ocean response in transient simulations of
596 the last deglaciation dominated by underlying ice-sheet reconstruction and method of meltwater
597 distribution, Geophys. Res. Lett., 49, e2021GL096767, https://doi.org/10.1029/2021GL096767, 2022.

598 Larsson, S.A., Kylander, M.E., Sannel, A.B.K., and Hammarlund, D.: Synchronous or not? The timing of the
599 Younger Dryas and Greenland Stadial-1 reviewed using tephrochronology. Quaternary, 5, 19,
600 https://doi.org/10.3390/quat5020019, 2022.

601 Liu, M., Prentice, I.C., ter Braak, C.J.F., and Harrison, S.P.: An improved statistical approach for reconstructing
602 past climates from biotic assemblages, Proc. Roy. Soc. A: Math., Phy. Eng. Sci., 476, 20200346.
603 https://doi.org/10.1098/rspa.2020.0346, 2020.

604 Liu, M., Shen, Y., González-Sampériz, P., Gil-Romera, G., ter Braak, C.J.F. Prentice, I.C., and Harrison, S.P.:
605 Holocene climates of the Iberian Peninsula, Clim. Past, 19, 803-834, https://doi.org/10.5194/cp-19-803-
606 2023, 2023.

607 Liu, Z., Otto-Bliesner, B. L., He, F., Brady, E. C., Tomas, R.. Clark, P. U., Carlson, A. E., Lynch-Stieglitz, J., Curry,
608   W., Brook, E., Erickson, D., Jacob, R., Kutzbach, J., and Cheng, J.: Transient Simulation of Last Deglaciation

609   with a New Mechanism for Bolling-Allerod Warming, Science, 325, 310-314,
610   doi:10.1126/science.1171041, 2009.

611

612 Magyari, E.K., Pál, I., Vincze, I., Veres, D., Jakab, G., Braun, M., Szalai, Z., Szabó, Z., and Korponai, J.: Warm
613 Younger Dryas summers and early late glacial spread of temperate deciduous trees in the Pannonian Basin
614 during the last glacial termination (20-9 kyr cal BP), Quat. Sci. Rev., 225, 105980,
615 doi.org/10.1016/j.quascirev.2019.105980, 2019.

616 Marinova, E., Harrison, S.P., Bragg, F., Connor, S., de Laet, V., Leroy, S.A.G., Mudie, P., Atanassova, J.,
617 Bozilova, E., Caner, H., Cordova, C., Djamali, M., Filipova-Marinova, M., Gerasimenko, N., Jahns, S., Kouli, K.,
618 Kotthoff, U., Kvavadze, E., Lazarova, M., … and Tonkov, S.: Pollen-derived biomes in the Eastern
619 Mediterranean–Black Sea–Caspian-Corridor, J. Biogeog., 45, 484–499, https://doi.org/10.1111/jbi.13128,
620 2018.

621 Martin Calvo, M., and Prentice, I.C.: Effects of fire and CO_2 on biogeography and primary production in glacial
622 and modern climates, New Phytol., 208, 987–994. https://doi.org/10.1111/nph.13485, 2015.

623 Mauri, A., Davis, B.A.S., Collins, P.M., and Kaplan, J.O.: The influence of atmospheric circulation on the mid-
624 Holocene climate of Europe: a data–model comparison, Clim. Past, 10, 1925–1938,
625 https://doi.org/10.5194/cp-10-1925-2014, 2014.

626 Mauri, A., Davis, B.A.S., Collins, P.M., Kaplan, J.O.: The climate of Europe during the Holocene: a gridded
627 pollen-based reconstruction and its multi-proxy evaluation, Quat. Sci. Rev., 112, 109-127,
628 https://doi.org/10.1016/j.quascirev.2015.01.013, 2015.

629 Messager, E., Belmecheri, S., Von Grafenstein, U., Vincent, O., Voinchet, P., Puaud, S., Courtin-nomade, A.,
630 Guillou, H., Mgeladze, A., Dumoulin, J.-P., Mazuy, A., and Lordkipanidze, D.: Late Quaternary record of the
631 vegetation and catchment-related changes from Lake Paravani (Javakheti, South Caucasus), Quat. Sci. Rev.,
632 77, 125–140, https://doi.org/10.1016/j.quascirev.2013.07.011, 2013.

633 Mitchell, L., Brook, E., Lee, J., Buizert, C., and Sowers, T.: Constraints on the late Holocene anthropogenic
634 contribution to the atmospheric methane budget, Science, 342, 964–966, doi:10.1126/science.1238920,
635 2013.

636 New, M., Lister, D., Hulme, M., and Makin, I.: A high-resolution data set of surface climate over global land
637 areas, Clim. Res., 21, 1–25. https://doi.org/10.3354/cr021001, 2002.

638 Otto-Bliesner, B.L., Braconnot, P., Harrison, S.P., Lunt, D.J., Abe-Ouchi, A., Albani, S., Bartlein, P.J., Capron, E.,
639 Carlson, A.E., Dutton, A., Fischer, H., Goelzer, H., Govin, A., Haywood, A., Joos, F., LeGrande, A.N., Lipscomb,
640 W.H., Lohmann, G., Mahowald, N., … and Zhang, Q.: The PMIP4 contribution to CMIP6 – Part 2: Two
641 interglacials, scientific objective and experimental design for Holocene and Last Interglacial simulations,
642 Geosci. Model Dev., 10, 3979–4003. https://doi.org/10.5194/gmd-10-3979-2017, 2017.

643 Palmisano, A., Bevan, A., Kabelindde, A., Roberts, N., and Shennan, S.: Long-term demographic trends in
644 prehistoric Italy: Climate impacts and regionalised socio-ecological trajectories, J. World Prehist., 34, 381–
645 432, https://doi.org/10.1007/s10963-021-09159-3, 2021.

646 Patton, H., Hubbard, A., Andreassen, K., Auriac, A., Whitehouse, P.L., Stroeven, A.P., Shackleton, C.,
647 Winsborrow, M., Heyman, J., and Hall, A.M.: Deglaciation of the Eurasian ice sheet complex, Quat. Sci. Rev.,
648 169, 148–172, https://doi.org/10.1016/j.quascirev.2017.05.019, 2017.

649 Prentice, I.C., Harrison, S.P., and Bartlein, P.J.: Global vegetation and terrestrial carbon cycle changes after
650 the last ice age, New Phytol. 189, 988–998, https://doi.org/10.1111/j.1469-8137.2010.03620.x, 2011.

651 Prentice, I.C., Villegas-Diaz, R., and Harrison, S.P.: Accounting for atmospheric carbon dioxide variations in
652 pollen-based reconstruction of past hydroclimates, Glob. Planet. Change, 211, 103790.
653 https://doi.org/10.1016/j.gloplacha.2022.103790, 2022.

654 Prentice, I.C., Villegas-Diaz, R., and Harrison, S.P.: *codos: 0.0.2* (0.0.2). Zenodo.
655 https://doi.org/10.5281/ZENODO.5083309, 2022 (last accessed 17 April 2023)

656 Reimer, P., Austin, W. E. N., Bard, E., Bayliss, A., Blackwell, P. G., Ramsey, C. B., Butzin, M., Cheng, H.,
657 Edwards, R. L., Friedrich, M., Grootes, P. M., Guilderson, T. P., Hajdas, I., Heaton, T. J., Hogg, A. G., Hughen, K.
658 A., Kromer, B., Manning, S. W., Muscheler, R., … and Talamo, S.: The IntCal20 Northern Hemisphere
659 radiocarbon age calibration curve (0-55 cal kBP), Radiocarbon, 62, 725-757,
660 https://doi.org/10.1017/RDC.2020.41, 2020.

661 Renssen, H., Seppä, H., Heiri, O., Roche, D.M., Goosse, H., and Fichefet, T.: The spatial and temporal
662 complexity of the Holocene thermal maximum, Nat. Geosci. 2*, 411–414, https://doi.org/10.1038/ngeo513,
663 2009.

664 Richerson, P.J., Boyd, R., and Bettinger, R.L.: Was agriculture impossible during the Pleistocene but
665 mandatory during the Holocene? A climate change hypothesis, Am. Antiq., 66, 387–411,
666 https://doi.org/10.2307/2694241, 2001.

667 Roberts, N., Brayshaw, D., Kuzucuoğlu, C., Perez, R., and Sadori, L.: The mid-Holocene climatic transition in
668 the Mediterranean: Causes and consequences, Holocene, 21, 3–13,
669 https://doi.org/10.1177/0959683610388058, 2011.

670 Roberts, N., Cassis, M., Doonan, O., Eastwood, W., Elton, H., Haldon, J., Izdebski, A., and Newhard, J.: Not the
671 End of the World? Post-classical decline and recovery in rural Anatolia, Hum. Ecol., 46, 305–322,
672 https://doi.org/10.1007/s10745-018-9973-2, 2018.

673 Roberts, C.N., Woodbridge, J., Palmisano, A., Bevan, A., Fyfe, R., and Shennan, S.: Mediterranean landscape
674 change during the Holocene: Synthesis, comparison and regional trends in population, land cover and
675 climate, Holocene, 29, 923–937, https://doi.org/10.1177/0959683619826697, 2019.

676 Roffet-Salque, M., Marciniak, A., Valdes, P.J., Pawłowska, K., Pyzel, J., Czerniak, L., Krüger, M., Roberts, C.N.,
677 Pitter, S., Evershed, R.P.: Evidence for the impact of the 8.2-ky BP climate event on Near Eastern early
678 farmers, Proc Natl Acad Sci USA, 115, 8705-8709, doi: 10.1073/pnas.1803607115. 2018.

679 Ruddiman, W. F.: The anthropogenic greenhouse era began thousands of years ago, Clim. Change, 61, 261–
680 293, doi:10.1023/B:CLIM.0000004577.17928.fa, 2003.

681 Rymes, M.D., and Myers, D.R.: Mean preserving algorithm for smoothly interpolating averaged data. Solar
682 Energy, 71, 225–231, https://doi.org/10.1016/S0038-092X(01)00052-4, 2001.

683 Sadori, L., Jahns, S., and Peyron, O.: Mid-Holocene vegetation history of the central Mediterranean,
684 Holocene, 21, 117-129, https://doi.org/10.1177/0959683610377530, 2011.

685 Sidorenko, D., Goessling, H. f., von Koldunov, N., Scholz, P., Danilov, S., Barbi, D., Cabos, W., Gurses, O.,
686 Harig, S., Hinrichs, C., Juricke, S., Lohmann, G., Losch, M., Mu, L., Rackow, T., Rakowsky, N., Sein, D.,
687 Semmler, T., Shi, X., … and Jung, T.: Evaluation of FESOM2.0 coupled to ECHAM6.3: Preindustrial and

HighResMIP simulations, J. Adv. Model. Earth Syst., 11, 3794–3815, https://doi.org/10.1029/2019MS001696, 2019.

Singarayer, J.S., Valdes, P.J., Friedlingstein, P., Nelson, S., and Beerling, D.J.: Late Holocene methane rise caused by orbitally controlled increase in tropical sources, Nature, 470, 82– 85, doi:10.1038/nature09739, 2011.

Stocker, B.D., Yu, Z., Massa, C., and Joos, F.: Holocene peatland and ice-core data constraints on the timing and magnitude of CO_2 emissions from past land use, Proc. Natl. Acad. Sci., 114, 1492-1497, doi:10.1073/pnas.1613889114, 2017.

Vadsaria, T., Zaragosi, S., Ramstein, G., Dutay, J-C., Li, L., Siani, G., Revel, M., Obase, T., and Abe-Ouchi, A.: Freshwater influx to the Eastern Mediterranean Sea from the melting of the Fennoscandian ice sheet during the last deglaciation, Sci. Rep. 12, 8466, https://doi.org/10.1038/s41598-022-12055-1, 2022.

Villegas-Diaz, R., and Harrison, S. P.: The SPECIAL Modern Pollen Data Set for Climate Reconstructions, version 2 (SMPDSv2), University of Reading. Dataset, https://doi.org/10.17864/1947.000389, 2022. (last accessed 17 April 2023).

Villegas-Diaz, R., and Harrison, S.P.: *smpds:* The SPECIAL Modern Pollen Data Set for Climate Reconstructions (v2.0.0). Zenodo. https://doi.org/10.5281/ZENODO.6598832, 2022. (last accessed 17 April 2023)

Villegas-Diaz, R., Cruz-Silva, E., and Harrison, S.P.: ageR: Supervised Age Models [R]. Zenodo. https://doi.org/10.5281/zenodo.4636716, 2021 (last accessed 17 April 2023).

Villegas-Diaz, R., Prentice, I.C., and Harrison, S.P.: COdos: CO_2 Correction Tools [R]. SPECIAL Research Group. https://github.com/special-uor/codos, 2022. (last accessed 17 April 2023)

Wei, D., González-Sampériz, P., Gil-Romera, G., Harrison, S.P., and Prentice, I.C.: Seasonal temperature and moisture changes in interior semi-arid Spain from the last interglacial to the Late Holocene, Quat. Res., 101, 143–155. https://doi.org/10.1017/qua.2020.108, 2021.

Weiberg, E., Bevan, A., Kouli, K., Katsianis, M., Woodbridge, J., Bonnier, A., Engel, M., Finné, M., Fyfe, R., Maniatis, Y., Palmisano, A., Panajiotidis, S., Roberts, C. N., and Shennan, S.: Long-term trends of land use and demography in Greece: A comparative study, Holocene, 29, 742–760, https://doi.org/10.1177/0959683619826641, 2019.

Weninger, B., Alram-Stern, E., Bauer, E., Clare, L., Danzeglocke, U., Jöris, O., Kubatzki, C., Rollefson, G., Todorova, H., and van Andel, T.: Climate forcing due to the 8200 cal yr BP event observed at Early Neolithic sites in the eastern Mediterranean, Quat. Res., 66, 401-420, https://doi.org/10.1016/j.yqres.2006.06.009, 2006.

Yanchilina, A.G., Ryan, W.B.F., Kenna, T.C., and McManus, J.F.: Meltwater floods into the Black and Caspian Seas during Heinrich Stadial 1, Earth Sci. Rev., 198, 102931, https://doi.org/10.1016/j.earscirev.2019.102931, 2019.

Zeder, M.A.: The origins of agriculture in the Near East, Curr. Anthropol., 52), S221–S235, https://doi.org/10.1086/659307, 2011.

Zhang, Y., Renssen, H., and Seppä, H.: Effects of melting ice sheets and orbital forcing on the early Holocene warming in the extratropical Northern Hemisphere, Clim. Past, 12, 1119–1135. https://doi.org/10.5194/cp-12-1119-2016, 2016.

729 Zhang, Y., Renssen, H., Seppä, H., and Valdes, P. J.: Holocene temperature trends in the extratropical
730 Northern Hemisphere based on inter-model comparisons, J. Quat. Sci., 33, 464–476.
731 https://doi.org/10.1002/jqs.3027, 2018.

Figure and Table Captions

733 Figure 1. Distribution of pollen records used in the climate reconstructions. The colour coding shows the length
734 of the record.

735 Figure 2. Time series of reconstructed anomalies of mean temperature of the coldest month (MTCO) for
736 individual records. Entities are arranged by latitude (N-S). Information about the numbered individual sites
737 can be found in Supplementary Table 1.

738 Figure 3. Time series of reconstructed anomalies of mean temperature of the warmest month (MTWA) for
739 individual records. Entities are arranged by latitude (N-S). Information about the numbered individual sites
740 can be found in Supplementary Table 1.

741 Figure 4. Time series of reconstructed anomalies of plant available moisture, expressed as the ratio between
742 potential and actual evapotranspiration (α), at individual sites. A correction to account for the direct
743 physiological impacts of CO_2 on plant growth has been applied to the reconstructed α. Entities are arranged
744 by latitude (N-S). Information about the numbered individual sites can be found in Supplementary Table 1.

745 Figure 5. Composite changes in reconstructed mean temperature of the coldest month (MTCO), mean
746 temperature of the warmest month (MTWA), growing degree days above a base level of 0°C (GDD0), and plant
747 available moisture expressed as the ratio between potential and actual evapotranspiration (α). A correction
748 to account for the direct physiological impacts of CO_2 on plant growth has been applied to the reconstructions
749 of α. The dark blue line is a loess smoothed curve through the reconstruction with a window half width of 500
750 years; the green shading shows the uncertainties based on 1000 bootstrap resampling of the records. The
751 bottom panel shows the number of records used to create the composite through time.

752 Figure 6. Simulated regional changes in mean temperature of the coldest month (MTCO), mean temperature
753 of the warmest month (MTWA), growing degree days above a base level of 0°C (GDD0), and plant available
754 moisture expressed as the ratio between potential and actual evapotranspiration (α) in the EMBSeCBIO
755 domain from the TRACE-21K-I (green) and TRACE-21K-II (red) transient simulations. It is not possible to
756 calculate changes in α for the TRACE-21K-II simulation from the available data. Loess smoothed curves were
757 drawn using a window half width of 500 years, and the envelope was obtained through 1000 bootstrap
758 resampling of the sequences. The top panel shows the changes in summer and winter insolation (Wm^{-2}) at 40°
759 N.

760 Figure 7. Simulated regional changes in mean temperature of the coldest month (MTCO), mean temperature
761 of the warmest month (MTWA), and growing degree days above a base level of 0°C (GDD0) in the EMBSeCBIO
762 domain from the LOVECLIM transient simulation. It is not possible to calculate changes in α for the LOVECLIM
763 simulation from the available data. Loess smoothed curves were drawn using a window half width of 500
764 years, and the envelope was obtained through 1000 bootstrap resampling of the sequences.

765 Figure 8. Simulated regional changes in mean temperature of the coldest month (MTCO), mean temperature
766 of the warmest month (MTWA), and growing degree days above a base level of 0°C (GDD0) in the EMBSeCBIO
767 domain from the four PACMEDY simulations. The models are: Max Plank Institute Earth System Model (MPI),
768 Alfred Wagener Institute Earth System Model simulations (AWI), Institute Pierre Simon Laplace Climate Model

769   TR5AS simulation (IPSL-CM5) and Institute Pierre Simon Laplace Climate Model TR6A V simulation (IPSL-CM6).
770   Loess smoothed curves were drawn using a window half width of 500 years and the envelope was obtained
771   through 1000 bootstrap resampling of the sequences.

772   Figure 9. Comparison of regional composites of reconstructed seasonal temperatures from this study with
773   those derived from Mauri et al. (2015) and Herzschuh et al. (2022). Mauri et al. (2015 provide mean
774   temperature of the coldest month (MTCO) and mean temperature of the warmest month (MTWA)
775   reconstructions, which can be directly compared with our reconstructions. Herzschuh et al. (2022) only
776   provide reconstructions of July temperature. Our reconstructions are shown in blue, reconstructions based on
777   the Mauri et al. (2015) data set are shown in green, and reconstructions based on the Herzschuh et al.
778   reconstruction are shown in orange. The solid line is a loess smoothed curve through the reconstruction with
779   a window half width of 500 years; the shading shows the uncertainties based on 1000 bootstrap resampling
780   of the records.

781   Table 1. Leave-out cross-validation fitness of fxTWA-PLSv2 for mean temperature of the coldest month
782   (MTCO), mean temperature of the warmest month (MTWA), growing degree days above base level 0°C (GDD0)
783   and plant-available moisture (α) with p-spline smoothed fx estimation, using bins of 0.02, 0.02 and 0.002,
784   showing results for the selected component for each variable. RMSEP is the root-mean-square error of
785   prediction. p assesses whether using the current number of components is significantly different from using
786   one component less. The degree of overall compression is assessed by linear regression of the cross-validated
787   reconstructions onto the climate variable, where b1 and b1.se are the slope and the standard error of the
788   slope, respectively. The overall compression is reduced as the slope approaches 1. Full details for all the
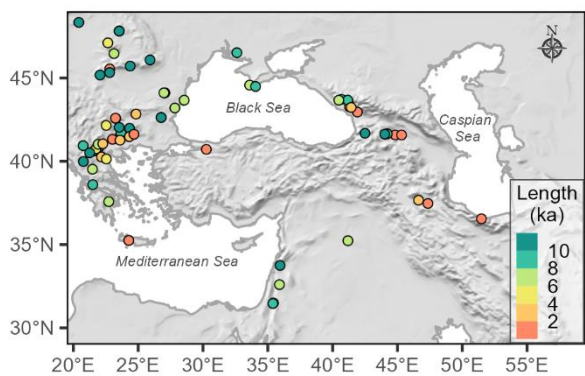789   components are given in Supplementary Table 4.

790

791

792

793

794

795 Figure 1. Distribution of pollen records used in the climate reconstructions. The colour coding shows the
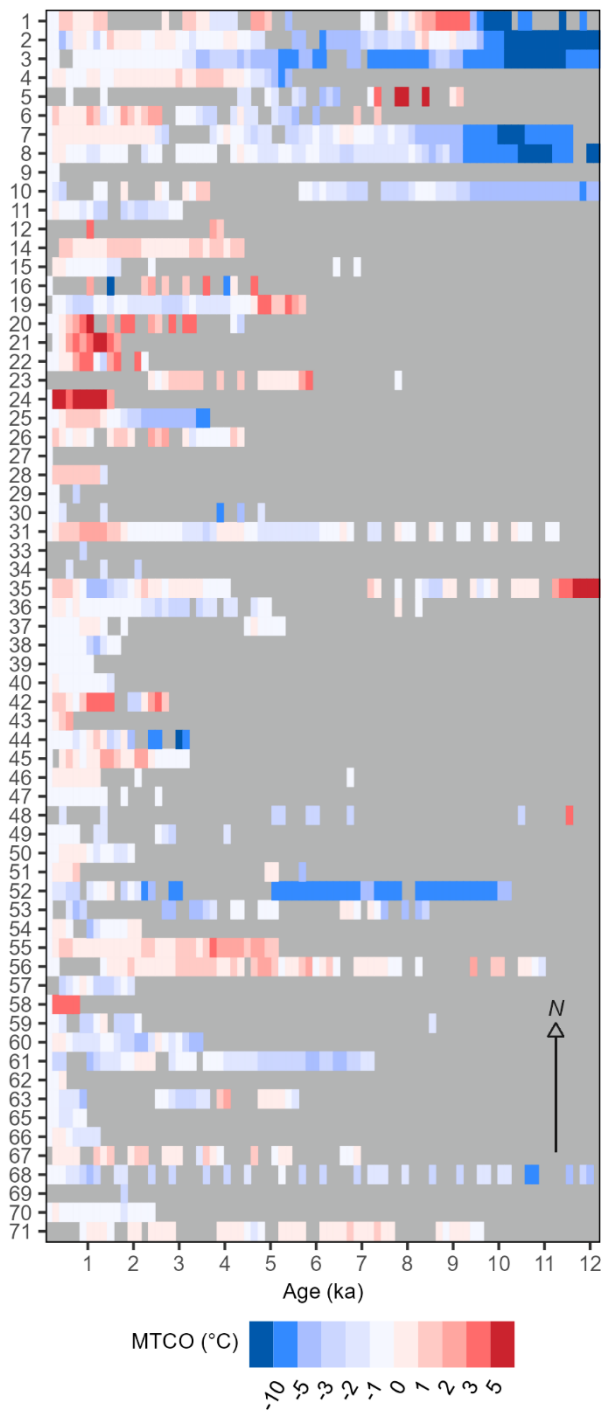796 length of the record.

797

798

799

800

801

802

803

804

Figure 2. Time series of reconstructed anomalies of mean temperature of the coldest month (MTCO) for
individual records. Entities are arranged by latitude (N-S). Information about the numbered individual sites
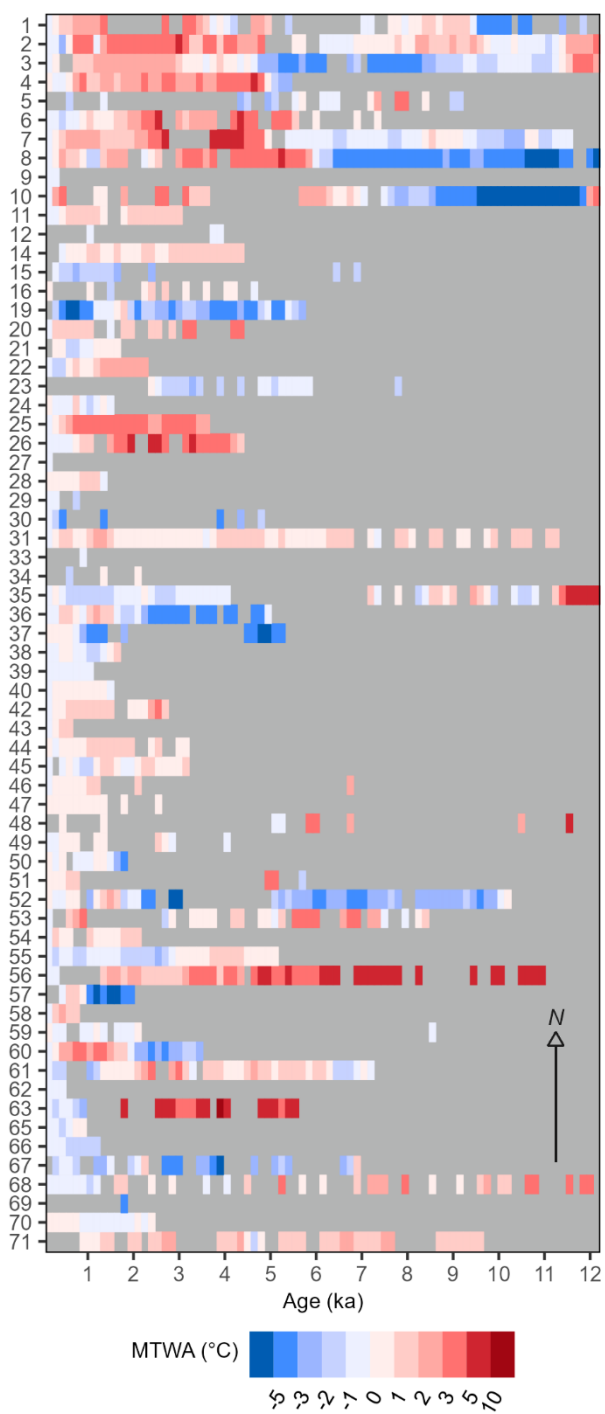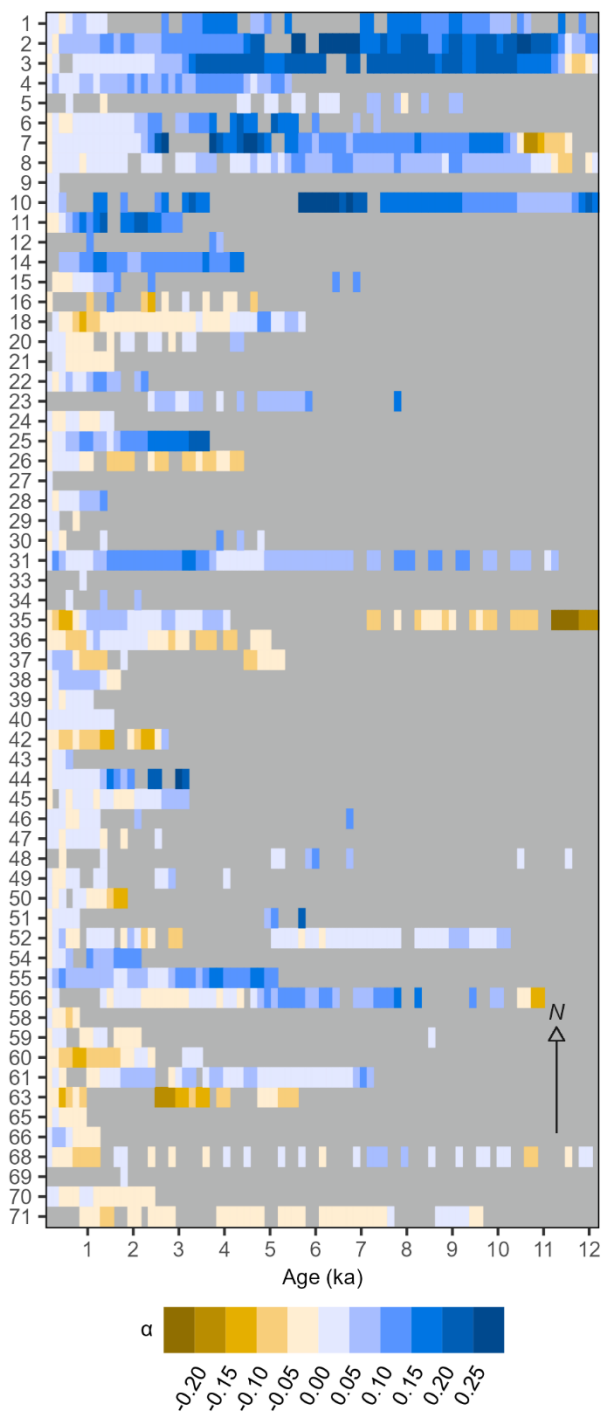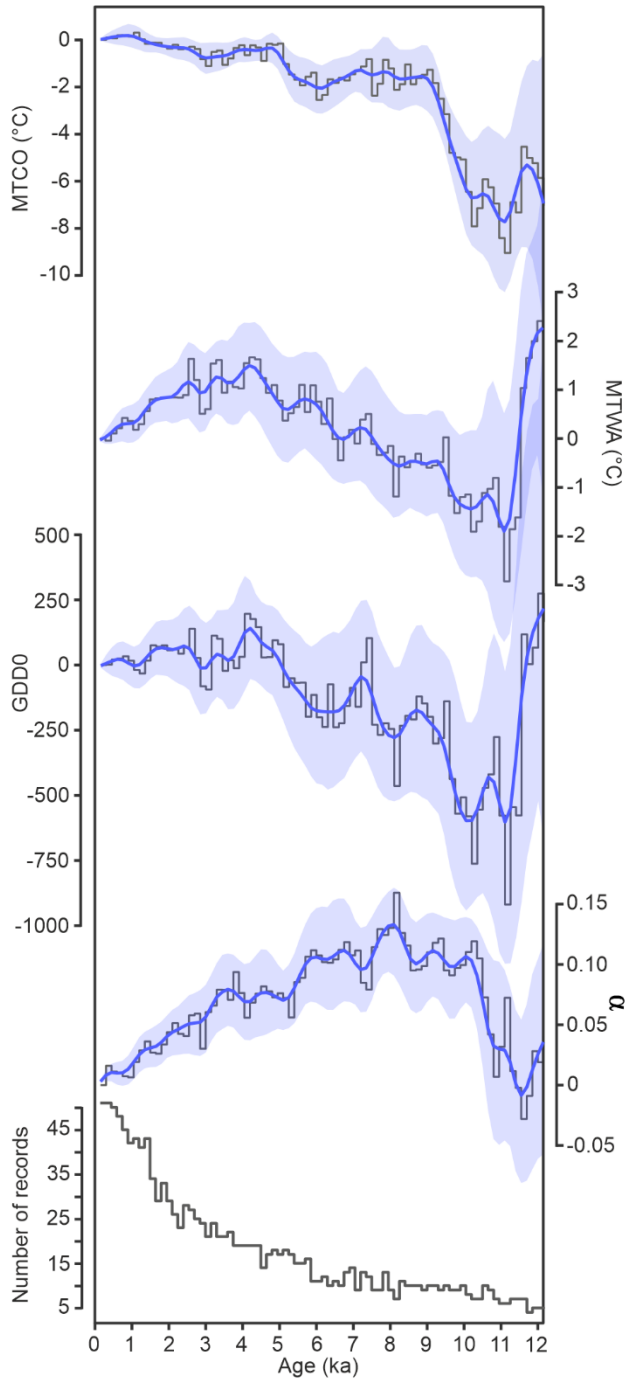can be found in Supplementary Table 1.

Figure 3. Time series of reconstructed anomalies of mean temperature of the warmest month (MTWA) for individual records. Entities are arranged by latitude (N-S). Information about the numbered individual sites can be found in Supplementary Table 1.

Figure 4. Time series of reconstructed anomalies of plant available moisture, expressed as the ratio between potential and actual evapotranspiration (α), at individual sites. A correction to account for the direct physiological impacts of CO_2 on plant growth has been applied to the reconstructed α. Entities are arranged by latitude (N-S). Information about the numbered individual sites can be found in Supplementary Table 1.

827 Figure 5. Composite changes in reconstructed mean temperature of the coldest month (MTCO), mean
828 temperature of the warmest month (MTWA), growing degree days above a base level of 0°C (GDD0), and
829 plant available moisture expressed as the ratio between potential and actual evapotranspiration (α). A
830 correction to account for the direct physiological impacts of CO_2 on plant growth has been applied to the
831 reconstructions of α. The dark blue line is a loess smoothed curve through the reconstruction with a window
832 half width of 500 years; the blue shading shows the uncertainties based on 1000 bootstrap resampling of the
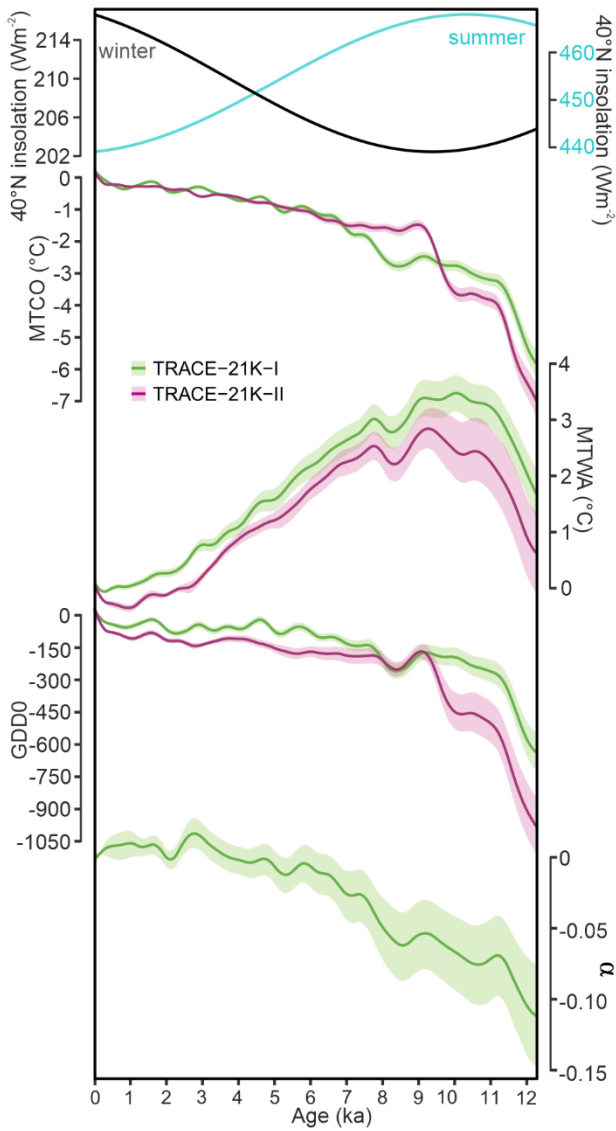833 records. The bottom panel shows the number of records used to create the composite through time.
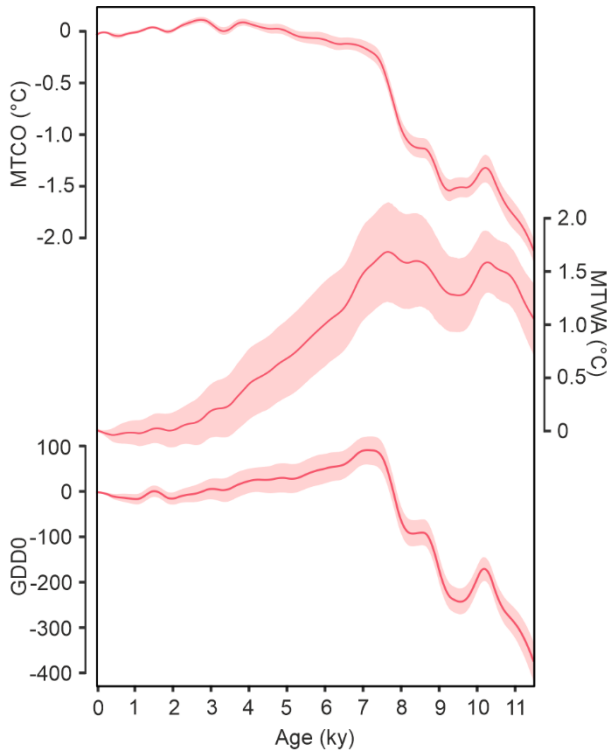

834

835

836

Figure 6. Simulated regional changes in mean temperature of the coldest month (MTCO), mean temperature of the warmest month (MTWA), growing degree days above a base level of 0°C (GDD0), and plant available moisture expressed as the ratio between potential and actual evapotranspiration (α) in the EMBSeCBIO domain from the TRACE-21K-I (green) and TRACE-21K-II (red) transient simulations. It is not possible to calculate changes in α for the TRACE-21K-II simulation from the available data. Loess smoothed curves were drawn using a window half width of 500 years, and the envelope was obtained through 1000 bootstrap resampling of the sequences. The top panel shows the changes in summer and winter insolation (Wm^{-2}) at 40° N.

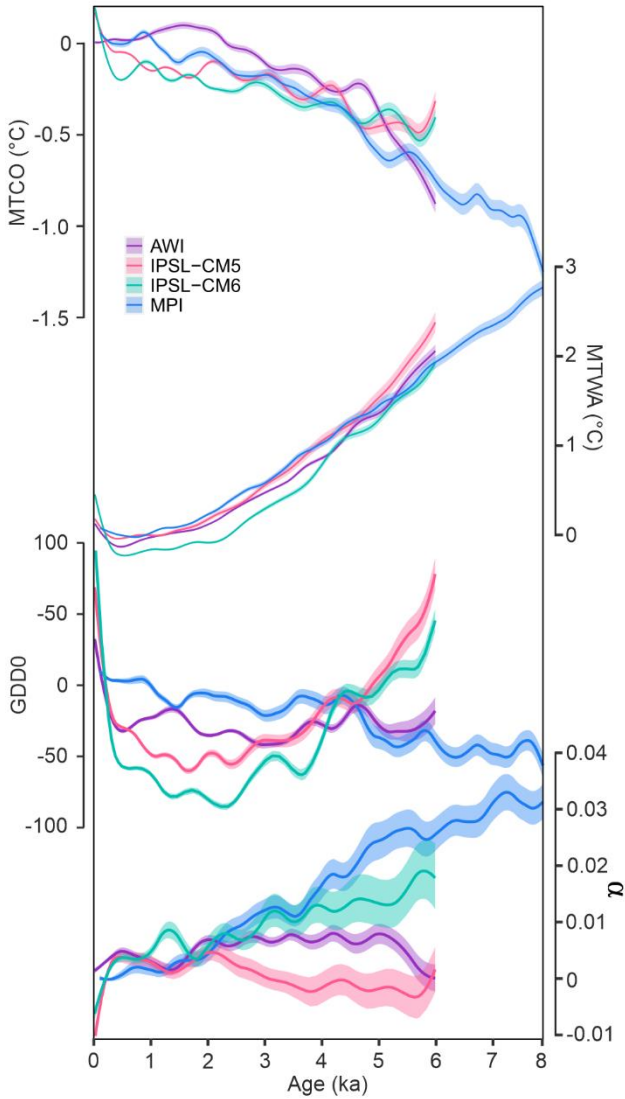Figure 7. Simulated regional changes in mean temperature of the coldest month (MTCO), mean temperature of the warmest month (MTWA), and growing degree days above a base level of 0°C (GDD0) in the EMBSeCBIO domain from the LOVECLIM transient simulation. It is not possible to calculate changes in α for the LOVECLIM simulation from the available data. Loess smoothed curves were drawn using a window half width of 500 years, and the envelope was obtained through 1000 bootstrap resampling of the sequences.
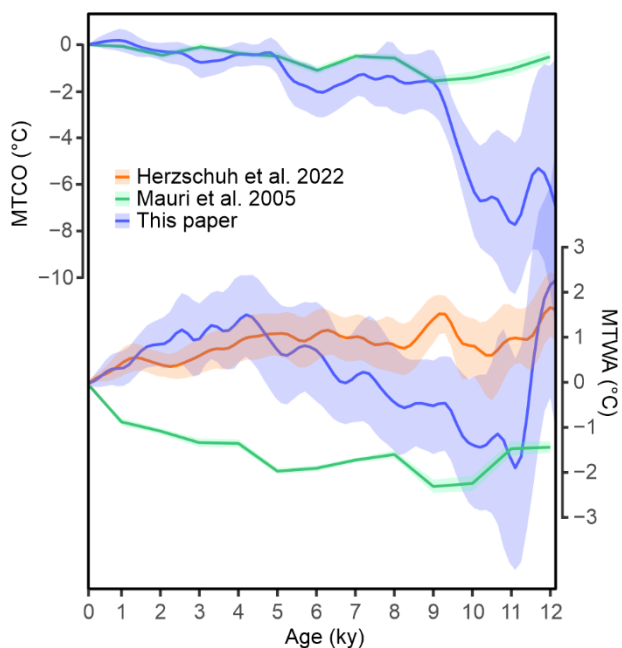
Figure 8. Simulated regional changes in mean temperature of the coldest month (MTCO), mean temperature of the warmest month (MTWA), and growing degree days above a base level of 0°C (GDD0) in the EMBSeCBIO domain from the four PACMEDY simulations. The models are: Max Plank Institute Earth System Model (MPI), Alfred Wagener Institute Earth System Model simulations (AWI), Institute Pierre Simon Laplace Climate Model TR5AS simulation (IPSL-CM5) and Institute Pierre Simon Laplace Climate Model TR6A V simulation (IPSL-CM6). Loess smoothed curves were drawn using a window half width of 500 years and the envelope was obtained through 1000 bootstrap resampling of the sequences.

Figure 9. Comparison of regional composites of reconstructed seasonal temperatures from this study with those derived from Mauri et al. (2015) and Herzschuh et al. (2022). Mauri et al. (2015 provide mean temperature of the coldest month (MTCO) and mean temperature of the warmest month (MTWA) reconstructions, which can be directly compared with our reconstructions. Herzschuh et al. (2022) only provide reconstructions of July temperature. Our reconstructions are shown in blue, reconstructions based on the Mauri et al. (2015) data set are shown in green, and reconstructions based on the Herzschuh et al. reconstruction are shown in orange. The solid line is a loess smoothed curve through the reconstruction with a window half width of 500 years; the shading shows the uncertainties based on 1000 bootstrap resampling of the records.

Table 1. Leave-out cross-validation fitness of fxTWA-PLSv2 for mean temperature of the coldest month (MTCO), mean temperature of the warmest month (MTWA), growing degree days above base level 0°C (GDD0) and plant-available moisture (α) with p-spline smoothed fx estimation, using bins of 0.02, 0.02 and 0.002, showing results for the selected component for each variable. RMSEP is the root-mean-square error of prediction. p assesses whether using the current number of components is significantly different from using one component less. The degree of overall compression is assessed by linear regression of the cross-validated reconstructions onto the climate variable, where b1 and b1.se are the slope and the standard error of the slope, respectively. The overall compression is reduced as the slope approaches 1. Full details for all the components are given in Supplementary Table 4.

Variable	Selected component	R2	Average bias	RMSEP	p	b1	b1.se
MTCO	4	0.73	-0.22	3.67	0.001	0.86	0.01
MTWA	2	0.63	-0.10	3.22	0.001	0.78	0.01
GDD0	2	0.69	56.46	880.33	0.001	0.79	0.01
α	2	0.73	-0.01	0.15	0.001	0.80	0.01